Static analysis of thin-walled beams accounting for nonlinearities

Static Analysis of Thin-Walled Beams Accounting for Nonlinearities

M. Petrolo, M.H. Nagaraj, E. Daneshkhah, R. Augello, and E. Carrera

MUL^2 Group, Department of Mechanical and Aerospace Engineering, Politecnico di Torino, Corso Duca degli Abruzzi 24, 10129 Torino, Italy

Revised version of Ms. No. JMES-21-0830

Author for correspondence:
M. Petrolo, Associate Professor
MUL^2 Group, Department of Mechanical and Aerospace Engineering,
Politecnico di Torino,
Corso Duca degli Abruzzi 24,
10129 Torino, Italy,
tel: +39 011 090 6845,
fax: +39 011 090 6899,
e-mail: marco.petrolo@polito.it

Abstract

This paper presents numerical results concerning the nonlinear analysis of thin-walled isotropic structures via 1D structural theories built with the Carrera Unified Formulation (CUF). Both geometrical and material nonlinearities are accounted for, and square, C- and T-shaped beams are considered. The results focus on equilibrium curves, displacement, and stress distributions. Comparisons with literature and 3D finite elements (FE) are provided to assess the formulation's accuracy and computational efficiency. It is shown how 1D models based on Lagrange expansions of the displacement field are comparable to 3D FE regarding the accuracy but require considerably fewer degrees of freedom.

Keywords: Carrera Unified Formulation, Geometrical and material nonlinear beams, Refined beam theories, Elastoplasticity

1 Introduction

Beam models have been developed extensively over the last few decades for the structural analysis of slender bodies, such as columns, arches, blades, aircraft wings, and bridges [1]. Beams have one dimension much larger than the other two and are primarily subjected to lateral loads, resulting in their reference axes' bending. Common loading conditions are extension, compression, bending, transverse shear, and twisting [2]. This paper focuses on two common sources of nonlinearity: geometrical and material. The former is due to the nonlinear strain-displacement relations, and the latter to the nonlinear constitutive behavior of the material of the system [3]. Some examples on the nonliear behavior of plates and shells can be found in [4–7]. Many studies have been focused on the elastoplastic analyses of beam-like structures [8–10]. Park and Lee [11] presented a 3D elastoplastic shear flexible beam element to solve geometrically nonlinear problems. Saje et al. [12] worked on the kinematically exact finite element model for elastoplastic arbitrarily curved beams. Pajunen [13] used kinematically exact finite beam element based on Reissner's stress resultant theory to solve large-deflection of elastoplastic beams. Mata et al. [14] studied the beam structures with nonlinear geometric and constitutive behavior and used thermodynamically consistent 3D constitutive laws to describe the material behavior. Challamel et al. [15] investigated the plasticity collapse of hardening-softening beams. Battini and Pacoste [16] investigated the plastic instabilities in the beams with arbitrary cross-sections. They presented a formulation for the 3D co-rotational elastic beam element with warping effects. The large deflection of elastoplastic frame structures has been studied in many works [17–20]. Among the others, the Generalized Beam Theory (GBT) is one of the most powerful approaches to investigate the nonlinear behavior of thin-walled structures [21, 22]. Abambres et al. [23] presented a formulation for the physically nonlinear analysis of thin-walled members with isotropic hardening based on the GBT. The same authors carried out a structural analysis of elastoplastic thin-walled members [24, 25].

The use of refined structural models helps reduce the computational cost of nonlinear analyses without compromising efficiency. The Carrera Unified Formulation (CUF) can generate any-order structural theory and, recently, has been extended to nonlinear problems [26–31]. Pagani and Carrera formulated a refined beam model based on the CUF to solve geometrically nonlinear problems. They presented the Fundamental Nucleus (FN) of the secant and tangent stiffness matrix and used the Newton-Raphson linearization scheme along with a path-following method [27]. The same authors investigated the large deflection and post-buckling of composite beams using the CUF, and layer-wise

kinematics [26]. Carrera et al. [29] carried out a nonlinear analysis on the elastoplastic thin-walled structures using the isotropically work-hardening von Mises constitutive model for the material nonlinearity. Petrolo et al. [28] presented a global-local approach based on the CUF considering physical nonlinearities to analyze elastoplastic thin-walled structures. Kaleel et al. [32] presented a numerical framework to simulate the progressive delamination in laminated structures based on 1D component-wise CUF models. The same authors [33] investigated the effect of kinematic enrichment for the nonlinear problems that included von Mises plasticity and cohesive interface modeling for delamination of composites. Nagaraj et al. [34] worked on the elastoplastic contact problems of compact and thin-walled metallic structures.

The present paper brings together, for the first time, the geometrical and material nonlinearities. In particular, Section 2 presents the CUF framework and the finite element formulation. Section 3 describer the nonlinear formulation. Sections 4 and 5 present the numerical results and their discussion.

2 Structural theories

By considering a generic beam with the cross-section domain in the x,z plane, and the axis along the y-direction, the displacement, stress, and strain vectors are expressed as:

$$\begin{aligned} \boldsymbol{u}(x,y,z) &= \{u_x\, u_y u_z\}^T \\ \boldsymbol{\sigma} &= \{\sigma_{xx}\ \ \sigma_{yy}\ \ \sigma_{zz}\ \ \sigma_{xz}\ \ \sigma_{yz}\ \ \sigma_{xy}\}^T \\ \boldsymbol{\varepsilon} &= \{\varepsilon_{xx}\ \ \varepsilon_{yy}\ \ \varepsilon_{zz}\ \ \varepsilon_{xz}\ \ \varepsilon_{yz}\ \ \varepsilon_{xy}\}^T \end{aligned} \tag{1}$$

In CUF, the 3D displacement field and its variation (δ) read:

$$\begin{aligned} \mathbf{u}(x,y,z) &= F_\tau(x,z)\mathbf{u}_\tau(y), \qquad \tau = 1,2,....,M \\ \delta\mathbf{u}(x,y,z) &= F_s(x,z)\delta\mathbf{u}_s(y), \qquad s = 1,2,....,M \end{aligned} \tag{2}$$

where F_τ and F_s represent the cross-section functions defined over the x,z plane, $\mathbf{u}_\tau$ is the generalized displacement vector, and M indicates the number of terms within the expansion. In this paper, Taylor Expansion (TE) and Lagrange Expansion (LE) cross-section functions are adopted to model the beam displacement field.

TE models are based on the Maclaurin polynomials. The order of the TE model (N) indicates the structural theory of the beam, and, in CUF, it is user input. For example, in the case of N=2, the

second-order displacement field is

$$
\begin{aligned}
u_x &= u_{x_1} + xu_{x_2} + zu_{x_3} + x^2u_{x_4} + xzu_{x_5} + z^2u_{x_6} \\
u_y &= u_{y_1} + xu_{y_2} + zu_{y_3} + x^2u_{y_4} + xzu_{y_5} + z^2u_{y_6} \\
u_z &= u_{z_1} + xu_{z_2} + zu_{z_3} + x^2u_{z_4} + xzu_{z_5} + z^2u_{z_6}
\end{aligned}
\tag{3}
$$

where u_{x_1} to u_{z_6} are the eighteen generalized displacement variables. The classical beam theories such as Euler–Bernoulli and Timoshenko models can be obtained as particular cases of linear TE model (N=1) [35]. On the other hand, LE models have pure displacements as unknown variables. Namely, they allow the users to employ Lagrange Points (LPs), where displacement variables are located. In this paper, nine-node LEs (L9) are employed, and they ensure a quadratic interpolation of the variables. A schematic representation of TE and LE models for a beam structure is shown in Fig.1.

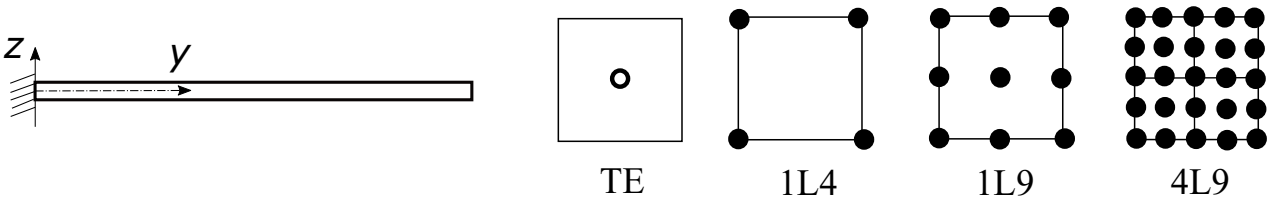

Figure 1: TE and LE cross-section functions for a square beam

The finite element method is used for the discretization of the beam axis. The generalized displacements (and their variation), lying in the y-direction, then become:

$$
\begin{aligned}
&\mathbf{u}_\tau(y) = N_i(y)\mathbf{q}_{\tau i} \qquad i = 1, 2, \ldots, N_n \\
&\delta\mathbf{u}_s(y) = N_j(y)\delta\mathbf{q}_{sj} \qquad j = 1, 2, \ldots, N_n
\end{aligned}
\tag{4}
$$

where N_i and N_j are the shape functions, and N_n is the number of nodes of each element. In this paper, four-node cubic finite elements (B4), ensuring a cubic interpolation. More information about Lagrange polynomials and shape functions can be found in [36]. By joining CUF (Eq. 2) and CUF (Eq. 4) formalisms, the 3D displacement field can be expressed as:

$$
\mathbf{u}(x, y, z) = F_\tau(x, z)N_i(y)\mathbf{u}_{\tau i} \tag{5}
$$

Higher-order expansions, e.g., Eq. 3, overcome the limitations of classical theories; for instance, they remove typical assumptions concerning the shear deformability and transverse stretching. Depending

on the problem at hand, the order assuring good accuracy may vary. CUF, via Eqs. 2 and 5, allows the choice of any-order expansions as the governing equations and finite element arrays are written in a way independent of the expansion order. The choice of the proper order for a given model can be made via a convergence analysis.

3 Geometrical and material nonlinearities

The Green-Lagrange nonlinear strain components are considered for the geometrical relations, as follows:

$$\boldsymbol{\epsilon} = \boldsymbol{\epsilon}_l + \boldsymbol{\epsilon}_{nl} = (\mathbf{b}_l + \mathbf{b}_{nl})\mathbf{u} \tag{6}$$

where $\mathbf{b}_l$ and $\mathbf{b}_{nl}$ are the following linear and nonlinear differential operators:

$$\mathbf{b}_l = \begin{bmatrix} \partial_x & 0 & 0 \\ 0 & \partial_y & 0 \\ 0 & 0 & \partial_z \\ \partial_z & 0 & \partial_x \\ 0 & \partial_z & \partial_y \\ \partial_y & \partial_x & 0 \end{bmatrix}, \qquad \mathbf{b}_{nl} = \begin{bmatrix} \frac{1}{2}(\partial_x)^2 & \frac{1}{2}(\partial_x)^2 & \frac{1}{2}(\partial_x)^2 \\ \frac{1}{2}(\partial_y)^2 & \frac{1}{2}(\partial_y)^2 & \frac{1}{2}(\partial_y)^2 \\ \frac{1}{2}(\partial_z)^2 & \frac{1}{2}(\partial_z)^2 & \frac{1}{2}(\partial_z)^2 \\ \partial_x\,\partial_z & \partial_x\,\partial_z & \partial_x\,\partial_z \\ \partial_y\,\partial_z & \partial_y\,\partial_z & \partial_y\,\partial_z \\ \partial_x\,\partial_y & \partial_x\,\partial_y & \partial_x\,\partial_y \end{bmatrix} \tag{7}$$

with $\partial_x = \dfrac{\partial(\cdot)}{\partial x}$, $\partial_y = \dfrac{\partial(\cdot)}{\partial y}$, and $\partial_z = \dfrac{\partial(\cdot)}{\partial z}$. By introducing the CUF (Eq. (2)) and FEM (Eq. (4)) relations into Eq. (6), the strain vector can be written in an algebraic form as follows:

$$\boldsymbol{\epsilon} = (\mathbf{B}_l^{\tau i} + \mathbf{B}_{nl}^{\tau i})\mathbf{q}_{\tau i} \tag{8}$$

where $\mathbf{B}_l^{\tau i}$ and $\mathbf{B}_{nl}^{\tau i}$ are the linear and nonlinear algebraic matrices with CUF and FEM formulations. Equation (8) allows writing the geometric relations in terms of the generalized nodal unknowns $\mathbf{q}_{\tau i}$. The explicit form of these two matrices are not reported here for the sake of brevity, but they are

reported in [27].

As far as the constitutive relation is concerned, the isotropic work-hardening von Mises constitutive model was considered. The von Mises model was used as it is one of the most used for metallic structures. Furthermore, given that this paper aims to explore the efficiency and accuracy of the proposed framework, the von Mises criterion is helpful as it allows the verification of the results against other papers from literature and commercial codes. Briefly, in case the elastic stress exceeds the yield limit of the material, the following scalar nonlinear equation is solved:

$$\overline{f}(\Delta\gamma) = q_{n+1}^{trial} - 3G\Delta\gamma - \sigma_y(\bar{\epsilon}_n^p + \Delta\gamma) \tag{9}$$

where q_{n+1}^{trial} is the trial von Mises stress at the increment t_{n+1}, G is the shear modulus, $\Delta\gamma$ is the unknown, σ_y is the yield stress, ϵ_n^p is the isotropic hardening parameter at the increment t_n and f is the con Mises yield locus, expressed as

$$f = q(\boldsymbol{\sigma}) - \sigma_y(\bar{\epsilon}_p) \tag{10}$$

where

$$q(\boldsymbol{\sigma}) = \sqrt{\frac{1}{2}\Big[(\sigma_{xx} - \sigma_{yy})^2 + (\sigma_{yy} - \sigma_{zz})^2 + (\sigma_{zz} - \sigma_{xx})^2 + 6(\sigma_{xy}^2 + \sigma_{xz}^2 + \sigma_{yz}^2)\Big]} \tag{11}$$

Equation (9) is solved using Newton-Raphson method and, with solution $\Delta\gamma$ at hand, $\boldsymbol{\sigma}$ and $\boldsymbol{\epsilon}$ are updated.

$$\begin{aligned} s_{n+1} &= \left(1 - \frac{\Delta\gamma 3G}{q_{n+1}^{trial}}\right) s_{n+1}^{trial} \\ \boldsymbol{\sigma}_{n+1} &= s_{n+1} + p_n^{trial}\mathbf{I} \\ \boldsymbol{\epsilon}_{n+1}^e &= \frac{1}{2G} s_{n+1} + \frac{1}{3}\epsilon_v^{e,trial}\mathbf{I} \\ \bar{\epsilon}_{n+1}^p &= \bar{\epsilon}_{n+1}^p + \Delta\gamma \end{aligned} \tag{12}$$

where $p_n^{trial}\mathbf{I}$ is the volumetric stress at increment t_n and $\frac{1}{3}\epsilon_v^{e,trial}$ is the volumetric component of the elastic trial strain, for more details [28, 37].

3.1 Nonlinear governing equations

For the quasi-static nonlinear problem, the principle of virtual work is herein recalled,

$$\delta L_{\text{int}} = \delta L_{\text{ext}} \tag{13}$$

where δL_{int} is the virtual variation of the strain energy and δL_{ext} is the virtual variation of the work of the external loads. The virtual variation of the internal work can be expressed as:

$$\delta L_{\text{int}} = \int_V \delta \boldsymbol{\epsilon}^T \boldsymbol{\sigma} \, \mathrm{d}V \tag{14}$$

where V is the initial volume of the undeformed structure. Introducing the geometrical (Eq. (8)) and constitutive relations (Eq. (12)) into Eq. (13), a set of nonlinear algebraic equation occurs. The Newton-Raphson incremental linearized scheme is employed as in Pagani and Carrera [26] and Carrera *et al.* [29]. The linearized strain-displacement operators and stress-strain relations are

$$\begin{aligned} \delta(\delta L_{\text{int}}) &= \int_V \delta(\delta \boldsymbol{\epsilon}^T \boldsymbol{\sigma}) \, \mathrm{d}V \\ &= \int_V \delta \boldsymbol{\epsilon}^T \delta \boldsymbol{\sigma} \, \mathrm{d}V \quad + \quad \int_V \delta(\delta \boldsymbol{\epsilon}^T) \boldsymbol{\sigma} \, \mathrm{d}V \\ &= \int_V \delta \boldsymbol{\epsilon}^T \mathbf{C}^{cep} \delta \boldsymbol{\epsilon} \, \mathrm{d}V \quad + \quad \int_V \delta(\delta \boldsymbol{\epsilon}^T) \boldsymbol{\sigma} \, \mathrm{d}V \end{aligned} \tag{15}$$

where $\mathbf{C}^{cep}$ is the elastoplastic tangent modulus (see [28, 37] for more details). Note that evaluating the second contribution on the right-hand side requires the linearization of the nonlinear geometrical relations. This term results in the geometric stiffness matrix $\mathbf{K}_\sigma$, which is not derived here for the sake of brevity, but interested readers are referred to [27]. By substituting the geometrical (Eq. (8)) and constitutive relations (Eq. (12)) into Eq. (15), the linearization of the internal strain energy holds

$$\delta(\delta L_{\text{int}}) = \delta \mathbf{q}_{sj}^T \, \mathbf{k}_T^{ij\tau s} \mathbf{q}_{\tau i} \tag{16}$$

where $\mathbf{k}_T^{ij\tau s}$ is the fundamental nucleus of the tangent stiffness matrix.

Using the Newton-Raphson linearization method, the resultant system of equations needs to be constrained. In this work, an arc-length path-following constraint is adopted. More details about the arc-length method adopted can be found in the works by Carrera [38] and Crisfield [39, 40].

4 Numerical results

The numerical results focus on three types of beam cross-sections: square, C-shaped, and T-shaped. For the C-shaped and T-shaped beams, the results of equilibrium curves are compared with the

available literature. Additionally, the stress distributions obtained by the various structural theories based on TE and LE models are discussed for the first numerical case, i.e. beam with a rectangular cross-section. Geometrical nonlinearity is considered in each assessment, and the assumed material behaviour is denoted using the labels *elastic* and *elastoplastic*.

4.1 Square beam

This section focuses on a square cantilever beam with a length of 1000 mm. The beam has an upward tip force at the free end; see Fig. 2. The properties of the material for this case are in Table 1: σ_0 and E_t are the yield stress and tangent modulus of the material with a bilinear stress-strain relation, respectively.

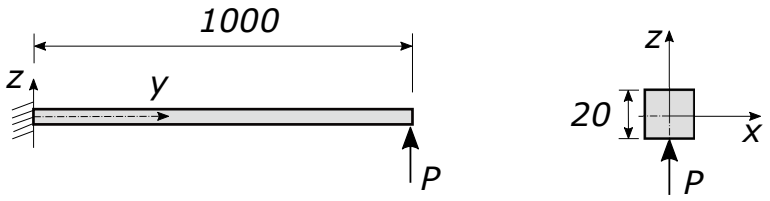

Figure 2: Schematic view of the square beam, all dimensions are in millimeters (mm)

Table 1: Material properties of the square beam

Material property	Value
Young's modulus	$E = 75\ GPa$
Tangent modulus	$E_t = E/10$
Poisson's ratio	$\nu = 0.33$
Yield stress	$\sigma_y = 500\ MPa$

The convergence analysis of equilibrium curves for the elastic case is in Fig. 3 with the applied force versus the vertical displacement of the square beam's tip end (0, 1000, -10). The first analysis case considered 20B4 elements along the beam axis, with 2L4, 1L9, and 4L9 over the cross-section. For the second analysis case, the cross-section expansion is 1L9, while the beam axis discretization ranges from 2B4 to 20B4. As 20B4 guarantees converged results, the subsequent analysis focuses on the effect of structural theories on equilibrium curves and stress distributions while keeping the finite element mesh constant. Table 2 shows the computational size of various models in terms of the number of DOF and the analysis time. The equilibrium curves for the elastic and elastoplastic

cases, as predicted using 1D CUF and reference 3D FE models, are in Fig. 4. Furthermore, Fig. 5 compares the two cases to highlight the effect of plasticity on the curves.

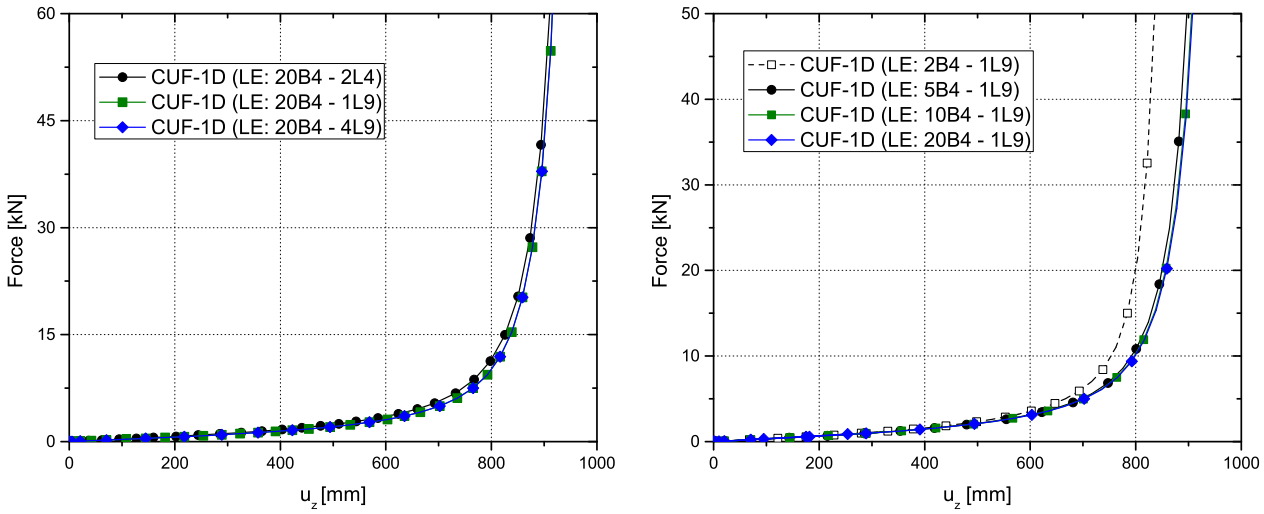

(a) **(b)**

Figure 3: Convergence analysis of equilibrium curves for the square beam with elastic behavior (a) effect of the structural theory (b) effect of the FE discretization

Table 2: Computational size of various models for the square beam

Model	DOF	Computational time* (s)
ABQ-3D Coarse	1869	83
ABQ-3D Medium	11001	194
ABQ-3D Refined	44085	546
CUF-1D (LE: 4L9)	4575	56
CUF-1D (LE: 9L9)	8967	101
CUF-1D (LE: 16L9)	14823	171
CUF-1D (TE: N=1)	549	138
CUF-1D (TE: N=2)	1098	483
CUF-1D (TE: N=3)	1830	2125

* The reported run-times refer to elastoplastic analyses performed on a laptop PC using a single core

The axial (σ_{yy}) and transverse shear (σ_{yz}) stress components, along the middle line of the cross-section (z-axis) near the clamped edge (y=75 mm) and at a load of 1100 N, are plotted in Fig. 6 and Fig. 7, respectively, for the case of the elastoplastic material. Similarly, the 2D stress distribution

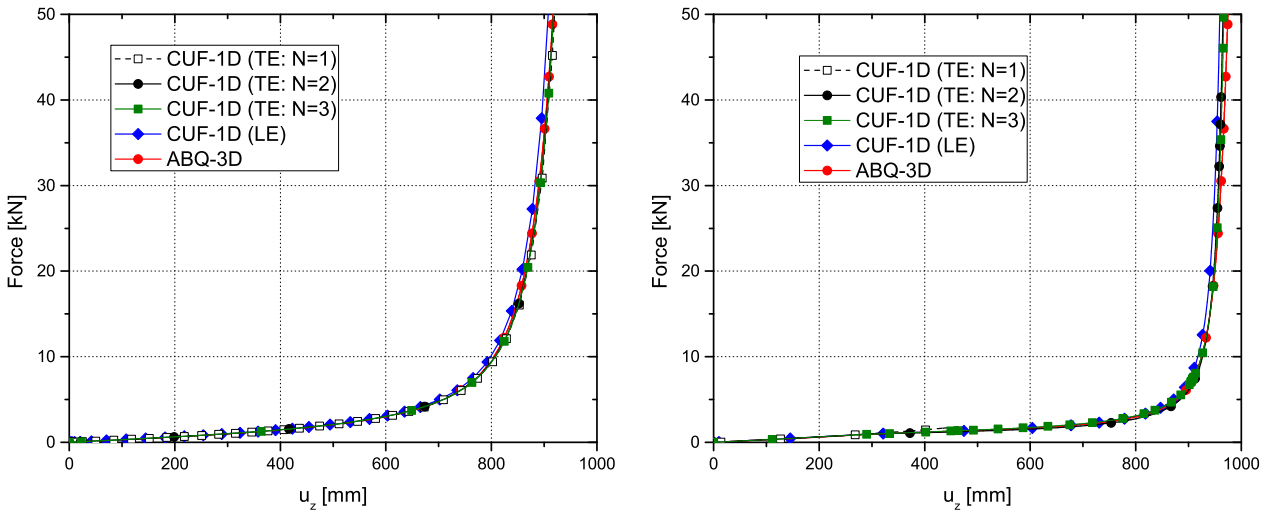

Figure 4: Equilibrium curves for the square beam based on various structural theories (a) elastic material (b) elastoplastic material

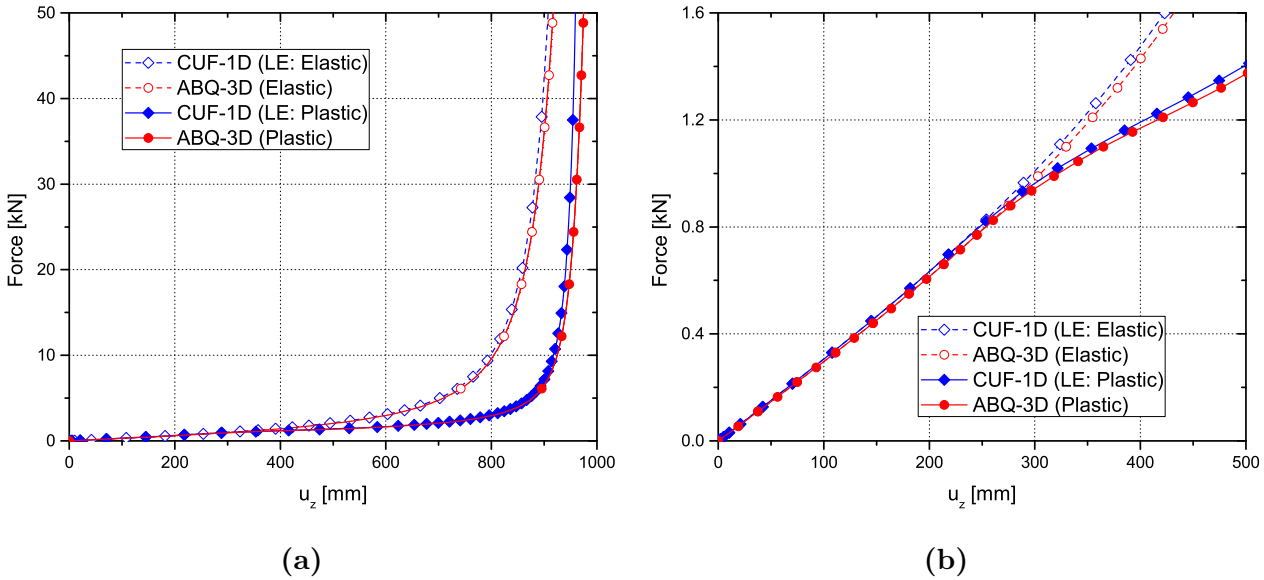

Figure 5: Effect of plasticity on equilibrium curves for the square beam (a) complete view (b) detailed view of plasticity initiation

of the two stress components at the same cross-section is shown in Fig. 8 and Fig. 9, respectively. Table 3 shows the transverse displacement (u_z) at the tip point of the beam (0, 1000, -10), the axial stress at (0, 75, 10), and the transverse shear stress at (0, 75, 0).

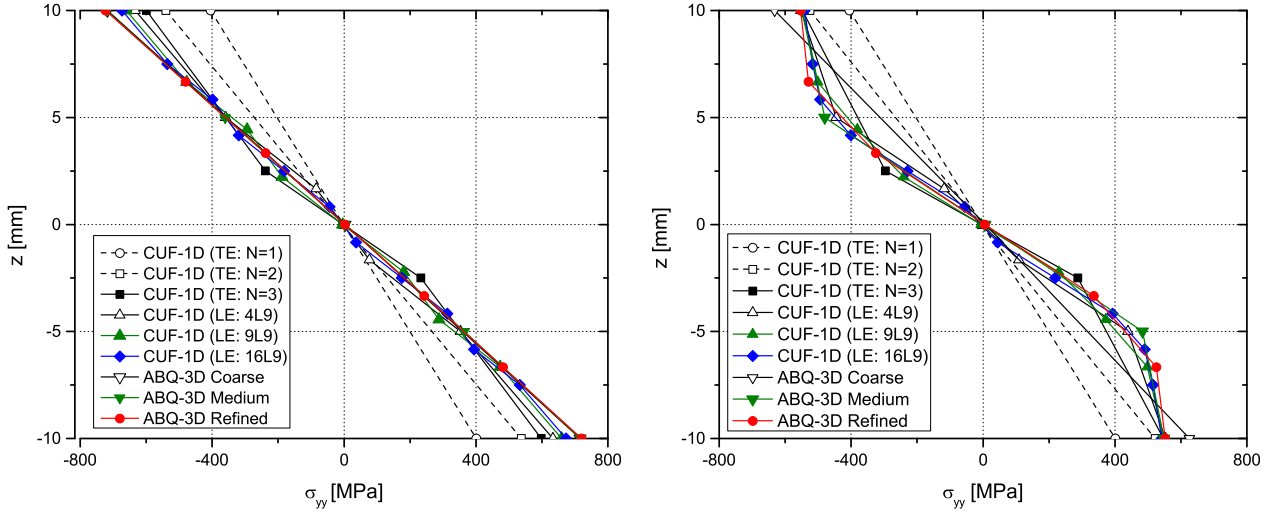

Figure 6: σ_{yy} at F=1100 N, x=0, y=75 mm of the square beam considering (a) elastic behavior of material (b) elastoplastic behavior of material

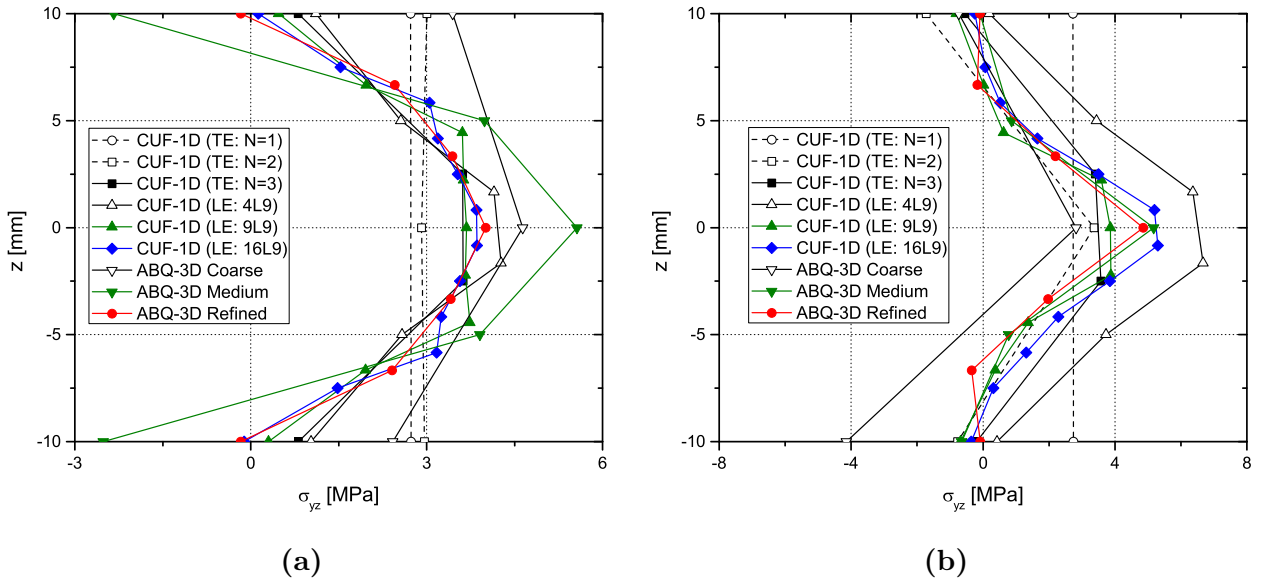

Figure 7: σ_{yz} at F=1100 N, x=0, y=75 mm of the square beam considering (a) elastic behavior of material (b) elastoplastic behavior of material

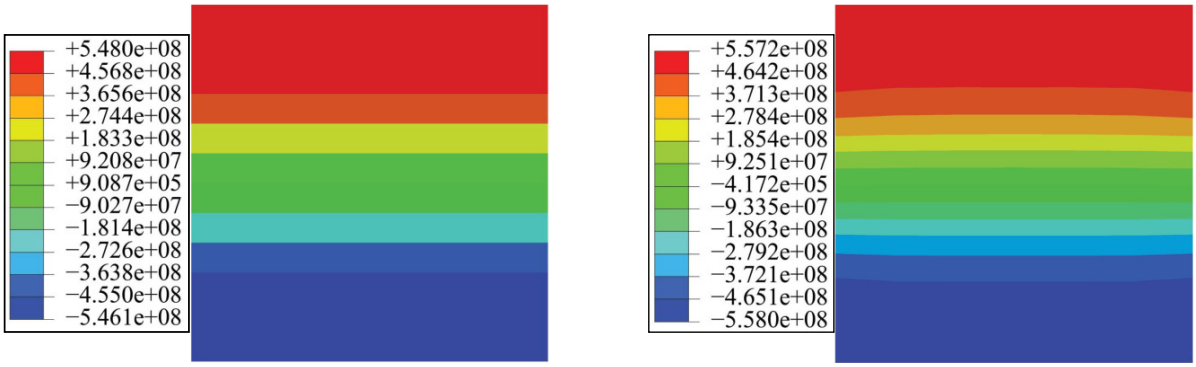

(a) **(b)**

Figure 8: 2D contour plots of σ_{yy} (Pa) with F=1100 N and y=75 mm of the square beam for the elastoplastic material based on (a) CUF-1D (LE: 16L9) (b) ABQ-3D Refined models

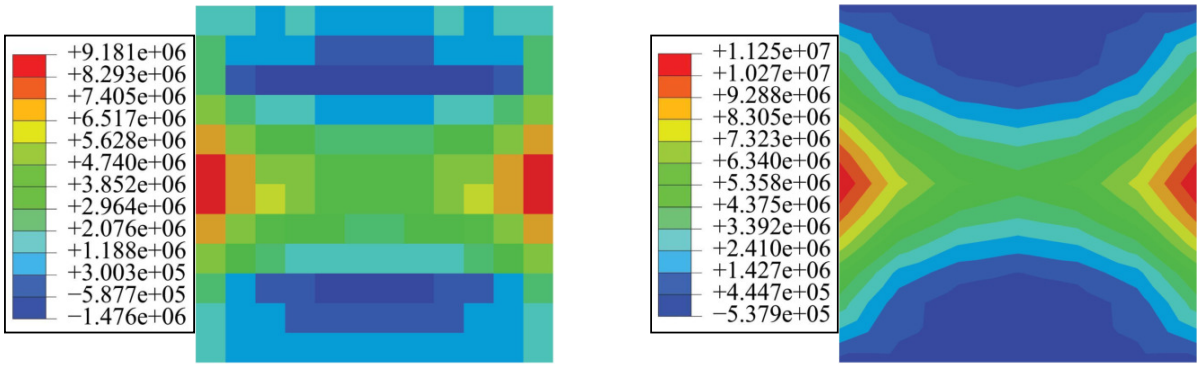

(a) **(b)**

Figure 9: 2D contour plots of σ_{yz} (Pa) with F=1100 N and y=75 mm of the square beam for the elastoplastic material based on (a) CUF-1D (LE: 16L9) (b) ABQ-3D Refined models

Table 3: u_z at the tip point of the square beam (0, 1000, -10), σ_{yy} at (0, 75, 10), and σ_{yz} at (0, 75, 0), with F=1100 N

	Elastic			Elastoplastic		
Model	u_z (mm)	σ_{yy} (MPa)	σ_{yz} (MPa)	u_z (mm)	σ_{yy} (MPa)	σ_{yz} (MPa)
ABQ-3D Coarse	328.4	-717.3	4.6	366.0	-632.0	2.8
ABQ-3D Medium	325.5	-719.9	5.5	363.4	-548.9	5.1
ABQ-3D Refined	324.5	-723.1	4.0	361.2	-553.0	4.8
CUF-1D (LE: 4L9)	321.6	-633.0	4.2	356.9	-552.1	6.5
CUF-1D (LE: 9L9)	321.7	-660.1	3.6	357.5	-544.9	3.8
CUF-1D (LE: 16L9)	321.7	-672.9	3.8	357.8	-541.0	5.2
CUF-1D (TE: N=1)	323.8	-404.5	2.7	331.1	-405.2	2.7
CUF-1D (TE: N=2)	322.5	-540.6	2.9	370.6	-524.9	3.3
CUF-1D (TE: N=3)	322.0	-599.5	3.6	359.8	-547.7	3.5

The following comments can be made according to the results of this section:

1. The convergence analysis for the equilibrium curves shows that, for the force-displacement curves, at least 10B4 and 1L9 are necessary.

2. Although CUF requires fewer DOF than 3D solid models, the equilibrium curves based on the 1D CUF LE models match well with the results obtained with 3D FE models.

3. All LE and TE models can predict the large displacements of the compact square beam within the elastic regime. However, lower-order TE models (N = 1,2) are not accurate enough when the load exceeds the yield limit.

4. A considerable difference near the bottom and the beam cross-section's top surface is visible between the axial stress distributions from lower-order models or coarse 3D meshes and refined models. Also, such differences seem more significant in the elastoplastic case and due to the presence of local plasticity requiring more complex kinematics modelings. In other words, the necessity of advanced structural theories for the elastoplastic problems is higher than the elastic case. Such requirements are even more stringent in the case of transverse shear stresses.

4.2 C-shaped beam

This section focuses on a C-shaped cantilever beam with a length of 900 cm [9], and is loaded by a point force at the free end, see Fig. 10. The properties of the material for this case are in Table 4, where σ_0 refers to the yield stress of elastic, perfectly-plastic material [16]. For all the following analyses, a 20B4 mesh was used.

Table 4: Material properties of the C-shaped beam

Material property	Value
Young's modulus	E=210 GPa
Poisson's ratio	ν=0.3
Yield stress	σ_y=360 MPa

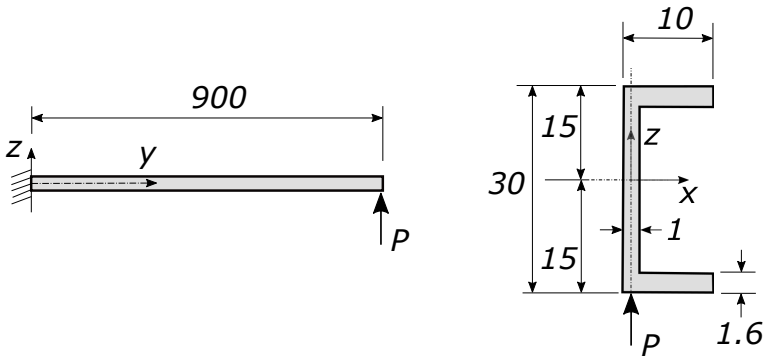

Figure 10: Schematic view of the C-shaped beam, all dimensions are in centimeters (cm)

Table 5 presents the various numerical models used for the current case. For the case of thin-walled structures with local deformation, the use of TE necessitates very high orders, and LE tends to be the preferable option [35]. The transverse displacement was evaluated at the point (0, 900, -15) to plot the equilibrium curves. Figure 11 compares the equilibrium curves for both the elastic and elastoplastic cases, obtained from the 1D-CUF (LE) model and reference numerical results from [16]. The 3D contour plots of displacement magnitude predicted by 1D CUF and 3D FE models are shown in Fig. 12.

Table 5: Computational size of various models for the C-shaped beam

Model	DOF	Computational time* (s)
ABQ-3D Coarse	9867	419
ABQ-3D Medium	125814	1193
ABQ-3D Refined	245049	2911
CUF-1D (LE: 5L9)	6039	322
CUF-1D (LE: 8L9)	9333	421
CUF-1D (LE: 13L9)	14823	730

* The reported run-times refer to elastoplastic analyses performed on a laptop PC using a single core

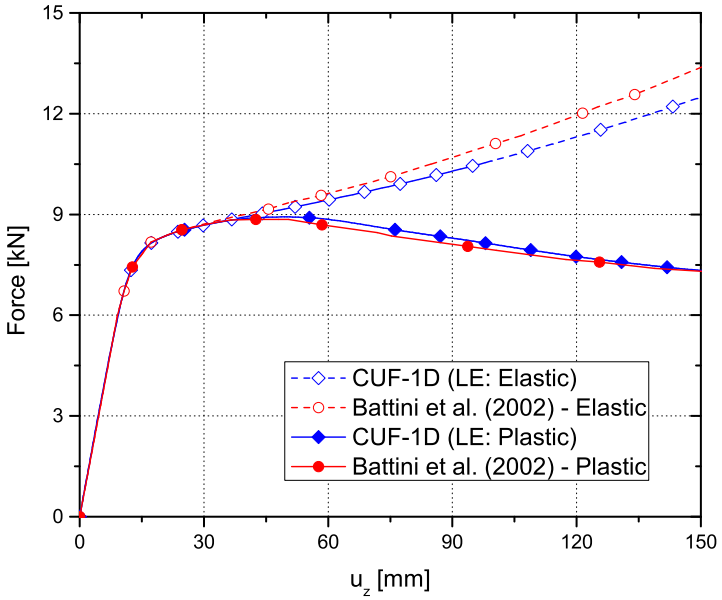

Figure 11: Equilibrium curves of the C-shaped beam with different material behaviors. Reference numerical results from [16]

The axial and transverse shear stresses along the z-axis at the point x=0, y=75 cm, for u_z=100 cm, are plotted in Figs. 13 and 14, respectively. Furthermore, for the elastoplastic material, the 2D contour plots of axial and transverse shear stresses for the corresponding cross-sections are shown in Figs. 15 and 16, respectively. Table 6 presents the axial stress σ_{yy} at (0, 75, 15), and the transverse shear stress σ_{yz} at (0, 75, 0), for u_z=100 cm.

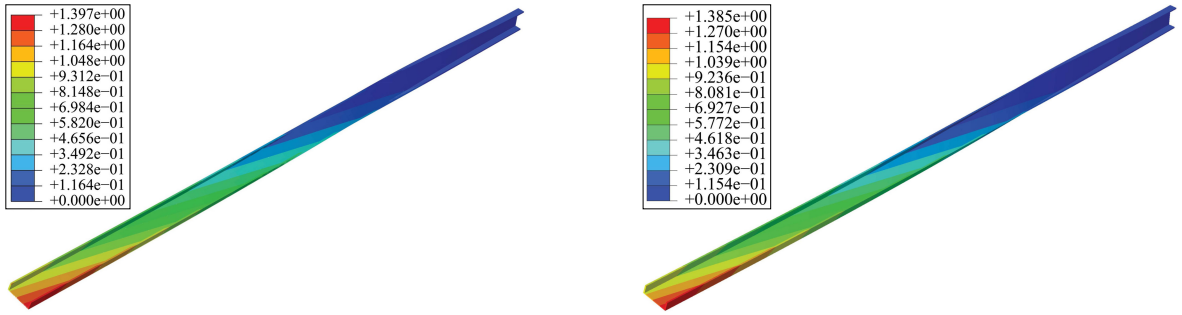

(a) **(b)**

Figure 12: 3D contour plots of the displacement (m) for the elastoplastic material, C-shaped beam based on (a) CUF-1D (LE: 13L9) (b) ABQ-3D Refined models

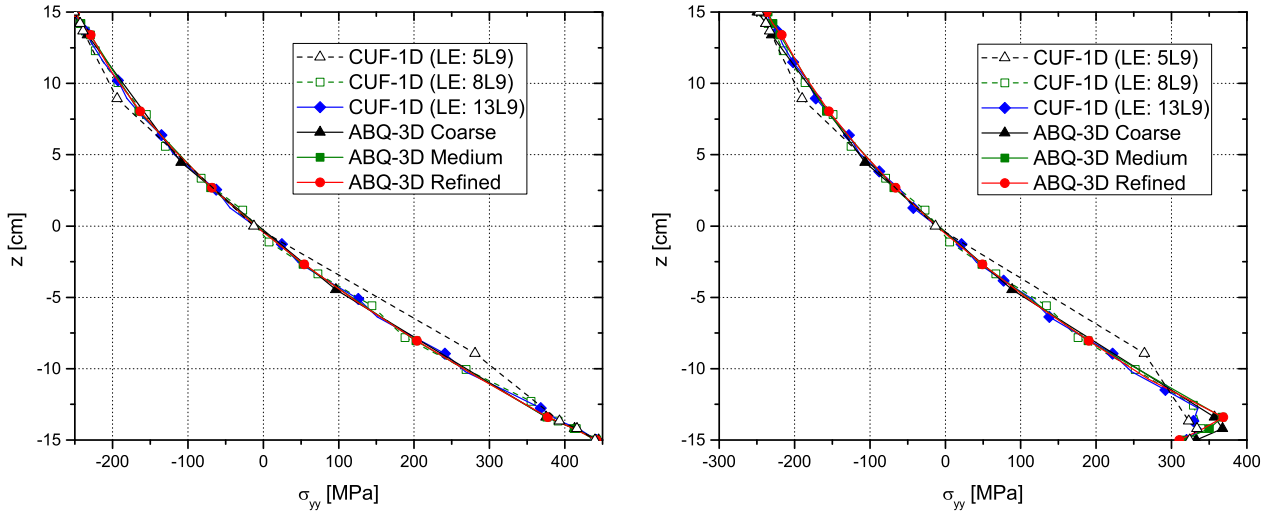

(a) **(b)**

Figure 13: σ_{yy} at x=0, y=75 cm for u_z=100 cm, C-shaped beam, considering (a) elastic material (b) elastoplastic material

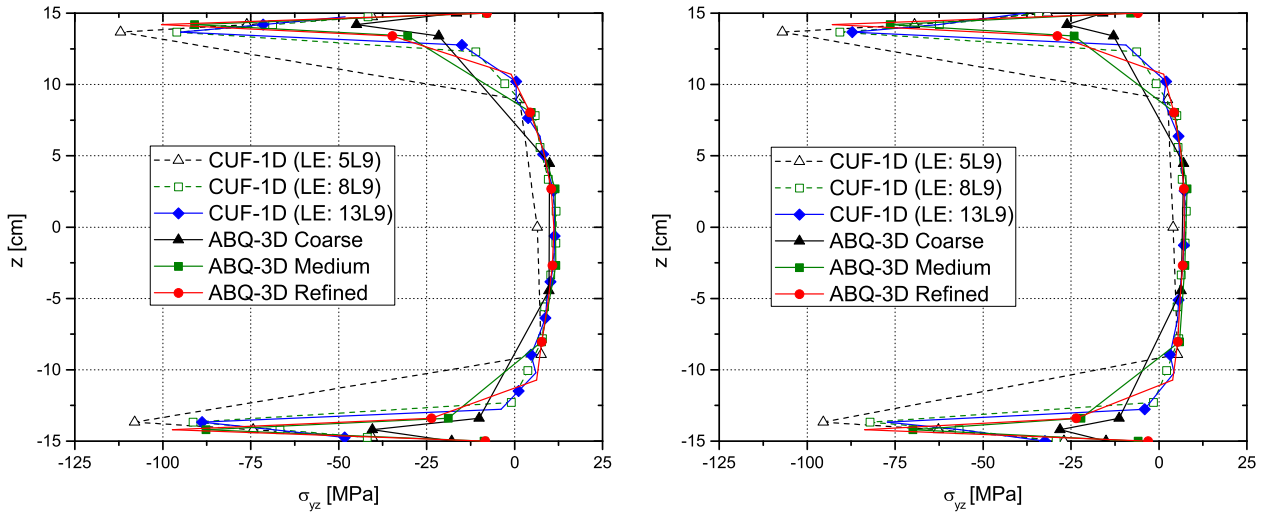

Figure 14: σ_{yz} at x=0, y=75 cm for u_z=100 cm, C-shaped beam, considering (a) elastic material (b) elastoplastic material

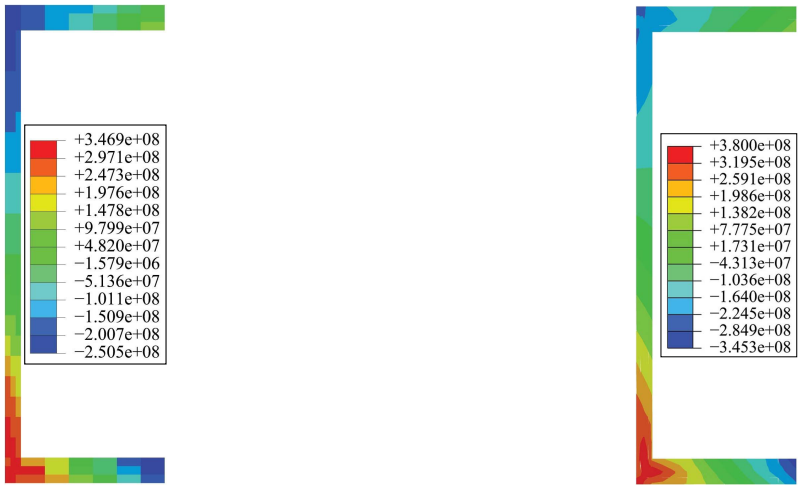

Figure 15: 2D contour plots of σ_{yy} for u_z=100 cm, at y=75 cm, elastoplastic material, C-shaped beam based on (a) CUF-1D (LE: 13L9) (b) ABQ-3D Refined models

(a) **(b)**

Figure 16: 2D contour plots of σ_{yz} for u_z=100 cm, at y=75 cm, elastoplastic material, C-shaped beam based on (a) CUF-1D (LE: 13L9) (b) ABQ-3D Refined models

Table 6: σ_{yy} at (0, 75, 15), and σ_{yz} at (0, 75, 0), for the C-shaped beam based on various structural theories and 3D FE discretizations for u_z=100 cm

	Elastic		Elastoplastic	
Model	σ_{yy} (MPa)	σ_{yz} (MPa)	σ_{yy} (MPa)	σ_{yz} (MPa)
ABQ-3D Coarse	-254.5	9.8	-249.2	6.6
ABQ-3D Medium	-249.5	11.6	-235.1	7.6
ABQ-3D Refined	-249.3	11.1	-236.9	7.1
CUF-1D (LE: 5L9)	-251.1	6.4	-247.1	4.0
CUF-1D (LE: 8L9)	-249.9	11.7	-242.0	7.6
CUF-1D (LE: 13L9)	-251.0	11.4	-238.0	7.2

The following comments can be made based on the results of this section:

1. The equilibrium curves based on the LE 13L9 model match well with the results obtained by Battini and Pacoste [16]. As known from previous works, classical and TE models cannot accurately predict the C-shaped beam's large displacements for either elastic or elastoplastic materials.

2. For the shear stress, the CUF-1D (LE: 5L9) and ABQ-3D Coarse models do not provide accurate results.

3. The DOF required by the 1D CUF models is one order of magnitude lower than that of 3D FE.

4.3 T-shaped beam

This section focuses on a T-shaped cantilever beam with a length of 1200 mm [16]. The free tip is loaded with a transverse force (P) and a lateral load F=P/1000, see Fig. 17. The properties of the material for this case are in Table 7, where σ_0 and E_t refer to the yield stress and tangent modulus of the material with a bilinear stress-strain relation, respectively [16].

Table 7: Material properties of the T-shaped beam

Material property	Value
Young's modulus	E=70 GPa
Tangent modulus	E_t=E/10
Poisson's ratio	ν=0.33
Yield stress	σ_y=500 MPa

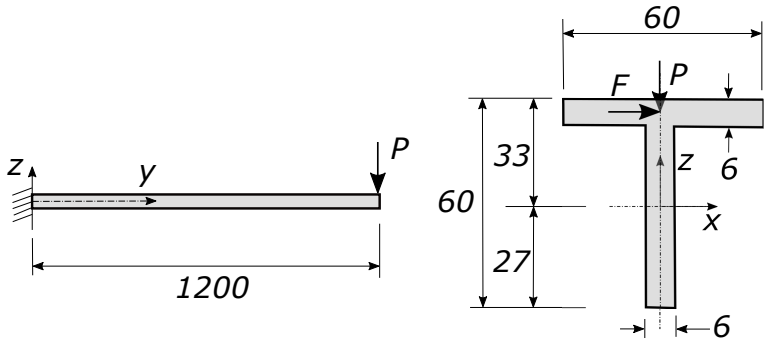

Figure 17: Schematic view of the T-shaped beam, all dimensions are in millimeters (mm)

Table 8 presents the computational size of all models adopted in the present assessment. Three CUF models are considered, with 5L9, 7L9, and 9L9 over the cross-section, respectively, and are discretized with 20B4 along the beam axis. The equilibrium curve predicted by the CUF model with 9L9 is plotted in Fig. 18, along with reference numerical results from [16]. A detailed view of the equilibrium curve is presented in Fig. 19. The 3D contour plots of the displacement are shown in Fig. 20, for a load value of 3400 N. The 2D contour plots of axial and shear stress components, for a load value of 3400 N, through the beam cross-section near the clamped edge (y=100 mm) are shown in Fig. 21 and Fig. 22, respectively. Table 9 lists the transverse displacement u_z at the free tip of

the beam (0, 1200, 30), the axial stress σ_{yy} at (0, 100, 33), and the shear stress σ_{yz} at (0, 100, 0), for a load value of 3400 N.

Table 8: Computational size of various numerical models used for the T-shaped beam

Model	DOF	Computational time* (s)
ABQ-3D Coarse	9393	241
ABQ-3D Medium	18453	477
ABQ-3D Refined	60549	1459
CUF-1D (LE: 5L9)	6039	142
CUF-1D (LE: 7L9)	8235	364
CUF-1D (LE: 9L9)	10431	484

* The reported run-times refer to elastoplastic analyses performed on a laptop PC using a single core.

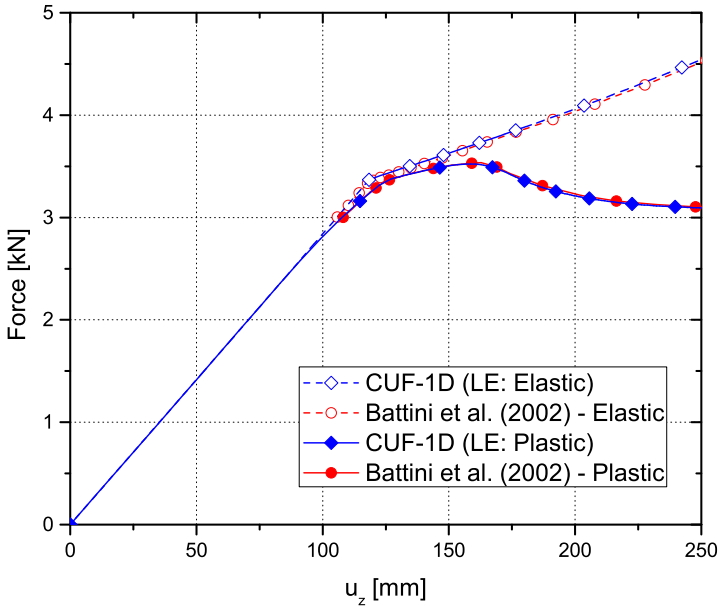

Figure 18: Equilibrium curves obtained from the CUF-1D (LE: 9L9) model considering elastic and elastoplastic material behavior. Reference numerical results from [16]

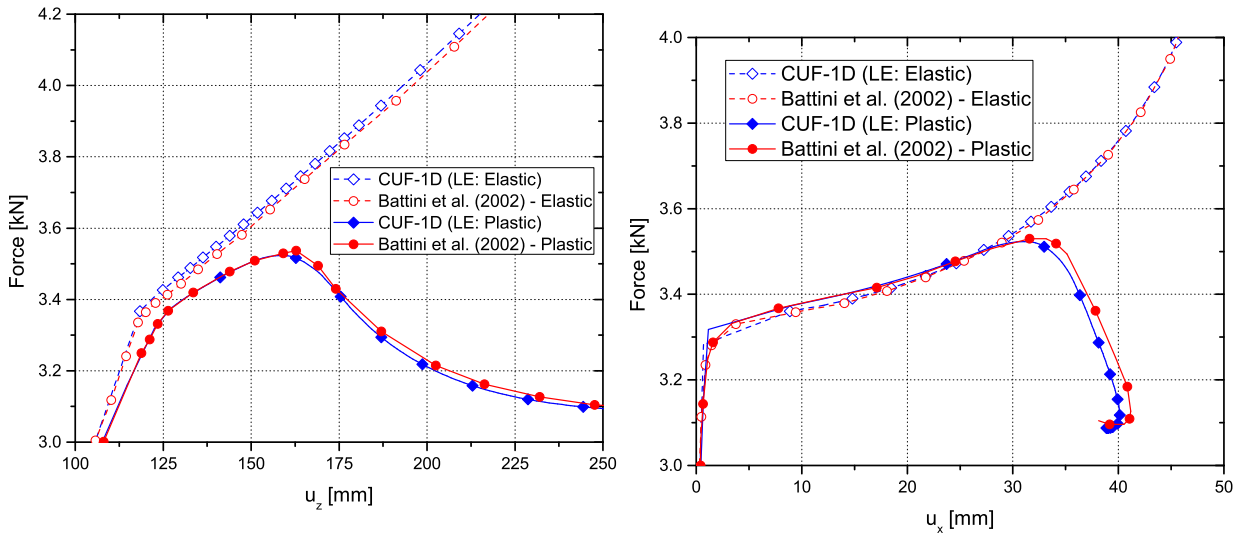

(a) **(b)**

Figure 19: Detailed view of the plasticity initiation for the T-shaped beam (a) force-vertical displacement (u_z) curve (b) force-lateral displacement (u_x) curve

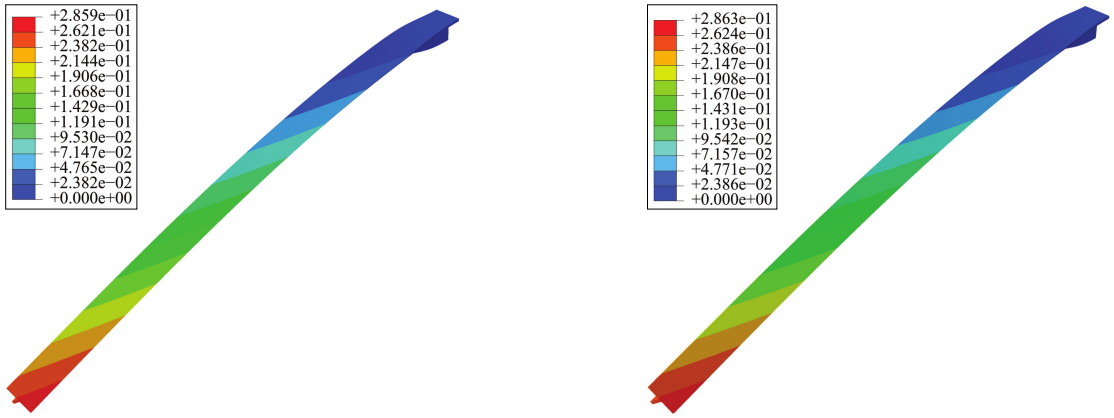

(a) **(b)**

Figure 20: 3D contour plots of the displacement (m) at the load of 3400 N for elastoplastic material based on (a) CUF-1D (LE: 9L9) (b) ABQ-3D Refined models

(a) **(b)**

Figure 21: 2D contour plots of σ_{yy} (Pa) at the load of 3400 N near the clamped edge (y=100 mm) for the elastoplastic material based on (a) CUF-1D (LE: 9L9) (b) ABQ-3D Refined models

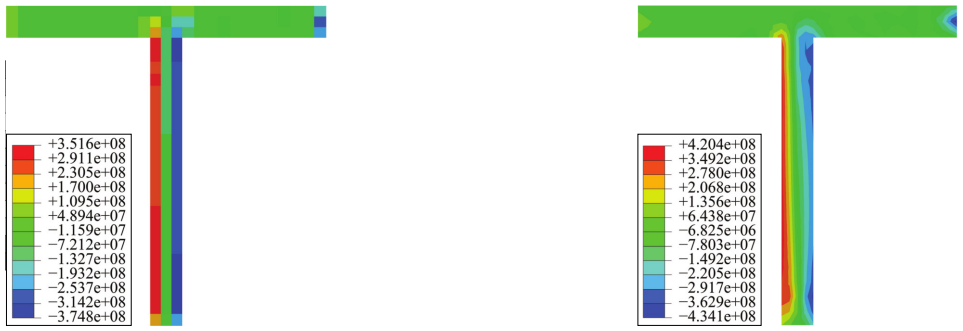

(a) **(b)**

Figure 22: 2D contour plots of σ_{yz} (Pa) at the load of 3400 N near the clamped edge (y=100 mm) for the elastoplastic material based on (a) CUF-1D (LE: 9L9) (b) ABQ-3D Refined models

Table 9: u_z at (0, 1200, 30), σ_{yy} at (0, 100, 33), and σ_{yz} at (0, 100, 0), T-shaped beam based at the load of 3400 N

	Elastic			Elastoplastic		
Model	u_z (mm)	σ_{yy} (MPa)	σ_{yz} (MPa)	u_z (mm)	σ_{yy} (MPa)	σ_{yz} (MPa)
ABQ-3D Coarse	122.2	264.7	-9.8	131.9	279.7	-10.7
ABQ-3D Medium	123.9	270.3	-10.4	133.4	286.9	-11.0
ABQ-3D Refined	126.5	279.5	-10.9	135.4	298.8	-12.4
CUF-1D (LE: 5L9)	121.7	259.9	-10.5	128.8	281.7	-10.8
CUF-1D (LE: 7L9)	123.0	261.5	-10.9	129.3	282.9	-12.1
CUF-1D (LE: 9L9)	124.1	267.9	-11.4	130.6	285.4	-12.5

The following comments can be made according to the results of this section:

1. The results for the T-shaped have similar characteristics to those of the C-shaped one.

2. Both transverse and lateral displacements were well captured. The latter, in particular, has a highly nonlinear equilibrium curve, necessitating a refined numerical model.

3. Stress distributions present high gradients along the cross-section and, in particular, the accurate modeling of shear stress requires refined 3D meshes or refined 1D CUF LE models.

5 Conclusions

The current work presents an investigation of compact and thin-walled isotropic beams considering both geometrical and physical nonlinearity. The focus is on using refined 1D structural theories

based on the Carrera Unified Formulation (CUF). For the first time, the geometrical and material nonlinearities have been considered simultaneously. Square, C-shaped, and T-shaped beams have been considered, and the results are presented in terms of equilibrium curves and stress distributions. Comparisons with results from literature and FE finite elements were made. The use of Lagrange-based 1D models has led to the same accuracy of 3D FE regarding equilibrium paths, displacement, and stress distributions. However, the use of 1D models can reduce the computational cost considerably as one order of magnitude fewer DOF was required. Future extensions should focus on high-velocity impact problems and progressive failure of composite structures.

References

[1] E. Carrera, A. Pagani, M. Petrolo, and E. Zappino. Recent developments on refined theories for beams with applications. *Mechanical Engineering Reviews*, 2(2):14–00298, 2015.

[2] A.H. Nayfeh and P.F. Pai. *Linear and nonlinear structural mechanics*. John Wiley & Sons, 2008.

[3] J.N. Reddy. *An introduction to nonlinear finite element analysis: with applications to heat transfer, fluid mechanics, and solid mechanics*. Oxford University Press, Oxford, 2014.

[4] N.D. Duc, P.H. Cong, and V.D. Quang. Nonlinear dynamic and vibration analysis of piezoelectric eccentrically stiffened FGM plates in thermal environment. *International Journal of Mechanical Sciences*, 115:711–722, 2016.

[5] P.H. Cong, N.D. Khanh, N.D. Khoa, and N.D. Duc. New approach to investigate nonlinear dynamic response of sandwich auxetic double curves shallow shells using tsdt. *Composite Structures*, 185:455–465, 2018.

[6] D.D. Nguyen, Q.Q. Tran, and D.K. Nguyen. New approach to investigate nonlinear dynamic response and vibration of imperfect functionally graded carbon nanotube reinforced composite double curved shallow shells subjected to blast load and temperature. *Aerospace Science and Technology*, 71:360–372, 2017.

[7] N.D. Duc and T.Q. Quan. Nonlinear response of imperfect eccentrically stiffened FGM cylindrical panels on elastic foundation subjected to mechanical loads. *European Journal of Mechanics-A/Solids*, 46:60–71, 2014.

[8] T.X. Yu and W. Johnson. The plastica: the large elastic-plastic deflection of a strut. *International Journal of Non-linear Mechanics*, 17(3):195–209, 1982.

[9] F. Gruttmann, R. Sauer, and W. Wagner. Theory and numerics of three-dimensional beams with elastoplastic material behaviour. *International Journal for Numerical Methods in Engineering*, 48(12):1675–1702, 2000.

[10] B. Štok and M. Halilovič. Analytical solutions in elasto-plastic bending of beams with rectangular cross section. *Applied Mathematical Modelling*, 33(3):1749–1760, 2009.

[11] M.S. Park and B.C. Lee. Geometrically non-linear and elastoplastic three-dimensional shear flexible beam element of von Mises-type hardening material. *International Journal for Numerical Methods in Engineering*, 39(3):383–408, 1996.

[12] M. Saje, G. Turk, A. Kalagasidu, and B. Vratanar. A kinematically exact finite element formulation of elastic-plastic curved beams. *Computers & structures*, 67(4):197–214, 1998.

[13] S. Pajunen. Large deflection elasto-plastic analysis of beams using kinematically exact elements. *Communications in numerical methods in engineering*, 16(7):497–504, 2000.

[14] P. Mata, S. Oller, and A.H. Barbat. Static analysis of beam structures under nonlinear geometric and constitutive behavior. *Computer methods in applied mechanics and engineering*, 196(45-48):4458–4478, 2007.

[15] N. Challamel, C. Lanos, and C. Casandjian. On the propagation of localization in the plasticity collapse of hardening–softening beams. *International Journal of Engineering Science*, 48(5):487–506, 2010.

[16] J.M. Battini and C. Pacoste. Plastic instability of beam structures using co-rotational elements. *Computer Methods in Applied Mechanics and Engineering*, 191(51-52):5811–5831, 2002.

[17] G. Shi and S.N. Atluri. Elasto-plastic large deformation analysis of space-frames: A plastic-hinge and stress-based explicit derivation of tangent stiffnesses. *International Journal for Numerical Methods in Engineering*, 26(3):589–615, 1988.

[18] G. Turkalj, J. Brnic, and J. Prpic-Orsic. ESA formulation for large displacement analysis of framed structures with elastic–plasticity. *Computers & structures*, 82(23-26):2001–2013, 2004.

[19] M. Shugyo. Elastoplastic large deflection analysis of three-dimensional steel frames. *Journal of Structural Engineering*, 129(9):1259–1267, 2003.

[20] R. He and H. Zhong. Large deflection elasto-plastic analysis of frames using the weak-form quadrature element method. *Finite Elements in Analysis and Design*, 50:125–133, 2012.

[21] R. Gonçalves and D. Camotim. Generalised beam theory-based finite elements for elastoplastic thin-walled metal members. *Thin-Walled Structures*, 49(10):1237–1245, 2011.

[22] N. Silvestre, M. Abambres, and D. Camotim. Influence of the deformation mode nature on the 1st order post-yielding strength of thin-walled beams. *Thin-Walled Structures*, 128:71–79, 2018.

[23] M. Abambres, D. Camotim, and N. Silvestre. Physically non-linear GBT analysis of thin-walled members. *Computers & Structures*, 129:148–165, 2013.

[24] M. Abambres, D. Camotim, N. Silvestre, and K.J. Rasmussen. GBT-based structural analysis of elastic–plastic thin-walled members. *Computers & Structures*, 136:1–23, 2014.

[25] M. Abambres, D. Camotim, and N. Silvestre. GBT-based elastic–plastic post-buckling analysis of stainless steel thin-walled members. *Thin-Walled Structures*, 83:85–102, 2014.

[26] A. Pagani and E. Carrera. Large-deflection and post-buckling analyses of laminated composite beams by Carrera Unified Formulation. *Composite Structures*, 170:40–52, 2017.

[27] A. Pagani and E. Carrera. Unified formulation of geometrically nonlinear refined beam theories. *Mechanics of Advanced Materials and Structures*, 25(1):15–31, 2018.

[28] M. Petrolo, M.H. Nagaraj, I. Kaleel, and E. Carrera. A global-local approach for the elastoplastic analysis of compact and thin-walled structures via refined models. *Computers & Structures*, 206:54–65, 2018.

[29] E. Carrera, I. Kaleel, and M. Petrolo. Elastoplastic analysis of compact and thin-walled structures using classical and refined beam finite element models. *Mechanics of advanced materials and structures*, 26(3):274–286, 2019.

[30] B. Wu, A. Pagani, M. Filippi, W.Q. Chen, and E. Carrera. Accurate stress fields of post-buckled laminated composite beams accounting for various kinematics. *International Journal of Non-Linear Mechanics*, 111:60–71, 2019.

[31] B. Wu, A. Pagani, M. Filippi, W.Q. Chen, and E. Carrera. Large-deflection and post-buckling analyses of isotropic rectangular plates by Carrera Unified Formulation. *International Journal of Non-Linear Mechanics*, 2019.

[32] I. Kaleel, E. Carrera, and M. Petrolo. Progressive delamination of laminated composites via 1D models. *Composite Structures*, page 111799, 2019.

[33] I. Kaleel, M. Petrolo, E. Carrera, and A.M. Waas. On the effectiveness of higher-order one-dimensional models for physically nonlinear problems. In *Advances in Predictive Models and Methodologies for Numerically Efficient Linear and Nonlinear Analysis of Composites*, pages 67–81. Springer, 2019.

[34] M.H. Nagaraj, I. Kaleel, E. Carrera, and M. Petrolo. Nonlinear analysis of compact and thin-walled metallic structures including localized plasticity under contact conditions. *Engineering Structures*, 203:109819, 2020.

[35] E. Carrera, M. Cinefra, M. Petrolo, and E. Zappino. *Finite element analysis of structures through Unified Formulation*. John Wiley & Sons, Chichester, West Sussex, UK, 2014.

[36] K.J. Bathe. *Finite element procedure*. Prentice Hall, Upper Saddle River, New Jersey, USA, 1996.

[37] E.A. de Souza Neto, D. Peric, and D.R. Owen. *Computational methods for plasticity: theory and applications*. Wiley, 2008.

[38] E. Carrera. A study on arc-length-type methods and their operation failures illustrated by a simple model. *Computers & structures*, 50(2):217–229, 1994.

[39] M.A. Crisfield. A fast incremental/iterative solution procedure that handles "snap-through". In *Computational Methods in Nonlinear Structural and Solid Mechanics*. Elsevier, Amsterdam, Netherlands, 1981.

[40] M.A. Crisfield. An arc-length method including line searches and accelerations. *International journal for numerical methods in engineering*, 19(9):1269–1289, 1983.